Adsorption of Water on Alkali Halide Surfaces Studied by Scanning Polarization Force Microscopy

M. Luna,[†] F. Rieutord,[‡] N. A. Melman,[§] Q. Dai,[||] and M. Salmeron*

Materials Sciences Division, Lawrence Berkeley National Laboratory, University of California, Berkeley, California 94720

Received: May 1, 1998

The adsorption of water on several alkali halide surfaces was studied using scanning polarization force microscopy. Water adsorption leads to an overall increase of surface potential and ionic mobility. At a critical humidity that is characteristic of each salt (NaCl, KCl, KBr, and KI), important changes in the rate of increase of the surface potential and ionic mobility occurred. Topographical changes occurred as well, in the form of step motion. These were observed to occur at a fast rate above the critical point, while little step motion occurred at lower humidity. Dissolution of the crystal (deliquescence) is observed at high humidity. Below the critical humidity, contact potential images indicate that preferential solvation of cations occurs at steps producing a large enhancement of the step contrast in the images.

Introduction

Adsorption of water on salt crystals plays a key role in many atmospheric and environmental chemistry processes. Micrometer and submicrometer size crystals of sodium chloride (and, to a lesser extent, potassium chloride) are major constituents of atmospheric aerosols, especially in marine areas. These aerosols play a fundamental role as condensation nuclei in cloud droplet formation.[1,2] Their surfaces can host a number of chemical reactions between atmospheric components. In order to better understand the first stages of drop growth in clouds and the dissolution processes that take place on these crystals, it is important to study water adsorption and the role of surface defects, such as steps, in detail. Although spectroscopic techniques are extremely valuable, the connection between adsorption and surface structure necessitates high-resolution microscopy. Unfortunately, although many surface characterization tools are available, most lack the lateral resolution that is necessary to directly visualize the mechanisms at play during adsorption. Scanning probe microscopies do have this resolution but are not suited, in their standard form, to study soft surfaces such as liquid-covered surfaces. Therefore, we have developed noncontact electrostatic atomic force microscopy (AFM) techniques with a resolution of a few tens of nanometers. This technique, which we call scanning polarization force microscopy (SPFM), was applied recently to study the structure and evolution of steps on the sodium chloride surface during water adsorption.[3] Here we extend these measurements to other alkali halide salts and further develop the technique to introduce time-dependent analysis. Several key surface parameters (both topographic and electrical) can be measured simultaneously to give further insight into the properties of the adsorbed water film.

Experimental Section

Instrument and Materials. All experiments were performed at room temperature (21 ± 1 °C) with a home-built AFM head and a commercial electronic control from RHK Technology, Inc. (STM 100). The microscope head is enclosed in a Plexiglas glovebox in which the relative humidity (RH) can be controlled from low values of 5−10% to high values of ∼80%. This was done by the combined use of desiccant materials and the flow of nitrogen bubbling through deionized water. RH was measured using an Omega hygrometer. The values quoted for the RH should be considered approximate within ±5%.

The NaCl, KCl, KF, and KBr single crystals used in the experiments were purchased from Optovac, EM Industries. They were cleaved parallel to the (001) planes inside the box at low humidity (10% RH). Data were collected as the sample was being exposed to increasing humidity for the first time after cleavage (first adsorption experiment). Occasionally second adsorption experiments (drying followed by water readsorption) were also run.

The cantilevers used (force constant of 0.58 N/m) were purchased from Digital Instruments. In order to make them conductive, they were covered with a 50 Å layer of Ti followed by a 500 Å layer of Pt or Au.

Operation Modes of the AFM. Operation of the AFM in the SPFM mode has previously been described in detail,[4,5] and thus only a brief description is given here. The AFM tip is biased to a few volts, such that strong attractive electrical forces are created between the tip and surface. These forces are in the nanonewton range at tip−surface distances of a few hundred angstroms. Because they originate from the polarization of the substrate charges, the local polarizability or dielectric constant, in addition to the tip−surface distance, are important. The electrostatic force also includes the effect of localized charges

---

* Corresponding author. Fax: 510-486-4995. E-mail: salmeron@stm.lbl.gov.

[†] Permanent address: Departamento de Física de la Materia Condensada, Facultad de Ciencias, C-III, Campus de Cantoblanco, Universidad Autónoma de Madrid, 28049 Madrid, Spain. E-mail: luna@ccuam3.sdi.uam.es.

[‡] Permanent address: Département de Recherche Fondamentale sur la Matière Condensée, Commissariat à l'Energie Atomique (CEA), 17 rue des Martyrs, 38054 Grenoble Cedex 9, France. E-mail: rieutord@cea.fr.

[§] Permanent address: Department of Physics, Eindhoven University of Technology, P.O. Box 513, 5600 MB Eindhoven, The Netherlands. E-mail: N.A.Melman@stud.tue.nl.

[||] Current address: IBM Corporation, 5600 Cottle Road, Mail Stop GG3A/006, San Jose, CA 95193. E-mail: qdai@vnet.ibm.com.

S1089-5639(98)02087-8 CCC: $15.00

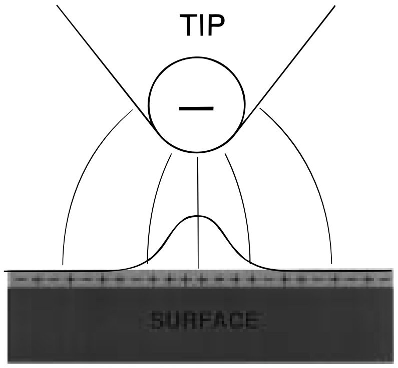

Figure 1. Schematic drawing illustrating the distribution of charge accumulated under the tip in response to the electric field. Solvated surface ions diffuse toward or away the projected tip position, depending on the bias.

or dipoles (surface potential). The force can be written in the form

$$F = -\frac{1}{2}\cdot\frac{\partial C}{\partial z}\cdot V_{\text{total}}^{2} \approx -4\pi\epsilon_0\cdot\frac{\epsilon - 1}{\epsilon + 1}\cdot f\left(\frac{R}{z}\right)\cdot(V + V_s)^2 \quad (1)$$

where C is the system capacitance, z the tip−sample distance, ϵ the local dielectric constant, and R the tip radius. The voltage difference V_{total} is separated into applied bias V and the local contact potential V_s. During imaging, the attractive force (lever deflection) is kept constant by the feedback control electronics. The function $f(R/z)$ depends on the geometry of the tip. For a point charge f, it is of the form R^2/z^2, but for a real tip the dependence is more complicated. In our experiments, the applied bias is dc positive or negative, or ac with a frequency of a few kilohertz.

Response Time Measurements

Whenever solvable ions are present at the surface, they generally provide the largest contribution to the polarization force at low frequencies. This was shown in detail in the case of mica exposed to humid environments[6] and results from the displacement of these ions toward or away from the projected tip position in response to the electric fields. The schematic drawing in Figure 1 illustrates the distribution of charge accumulated under the tip in this process. To measure the response time or ion mobility, the AFM tip is placed at a fixed position above the surface (~1000 Å), with the feedback control disabled. A square wave voltage is then applied to the tip, and the time evolution of the electrical polarization force is measured. The period of the square wave is adjusted so that a steady-state charge distribution has time to form, at which time the force reaches its maximum value. An example of this is shown in Figure 2. The top graph corresponds to the voltage applied to the cantilever, and the bottom one is the measured lever deflection, converted to force by multiplication by the lever spring constant. In steady state, the force is always attractive for both positive and negative bia voltages. Because of contact potential differences between the tip and surface, however, the force is not the same in the positive and negative cycles for a symmetrical square wave (see eq 1). For this reason, an offset voltage equal to the contact potential difference V_s is applied to compensate for this effect, as shown in Figure 2. Many curves such as those in Figure 2 are added together for improved signal-to-noise ratio. An example of such an averaged response curve is shown in Figure 3.

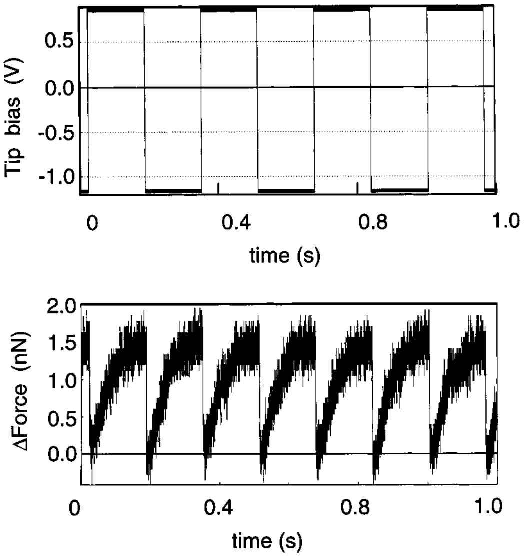

Figure 2. Top: Square wave voltage applied to the tip vs time. Bottom: corresponding changes in tip deflection (converted to force after multiplying by the lever spring constant). There is a net attractive force for both positive and negative bias. Note that the square wave voltage is not symmetric around zero. An offset is applied to compensate for the contact potential difference between the tip and surface. This offset is dependent on humidity.

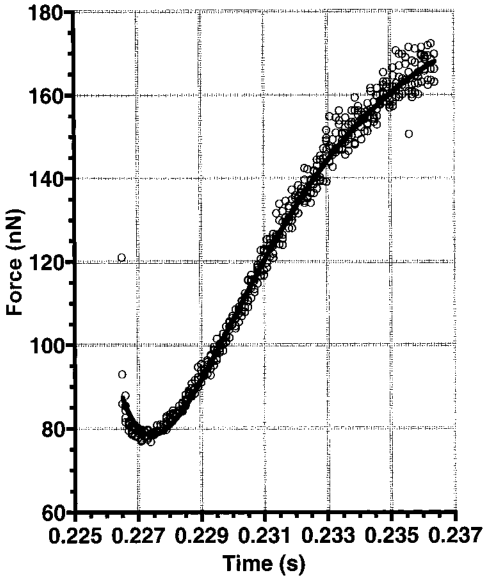

Figure 3. Averaged force vs time curve after a step change in tip voltage (see Figure 2). The curve is obtained by the addition of 20 cycles. The continuous line is a fit with a function of the type $a\cdot e^{-t/\tau} + b\cdot e^{-2t/\tau} + c$, as explained in the text.

A time constant τ characterizing the observed time evolution is extracted from the above curves by fitting a function of the form $a\cdot e^{-t/\tau} + b\cdot e^{-2t/\tau} + c$, as shown in Figure 3. This dependence will be discussed in more detail later. The results of many experiments for the four salts as a function of relative humidity are shown in Figure 4. In all cases, a similar behavior was observed: τ^{-1} increases smoothly and quasi-exponentially with humidity (note that the y axis is logarithmic) up to a specific humidity point A, where a change in the rate of increase is observed.

Contact Potential Measurements

The absorption of water also gives rise to a change in the surface potential. As mentioned above, differences in the contact potential between the tip and surface causes an asym-

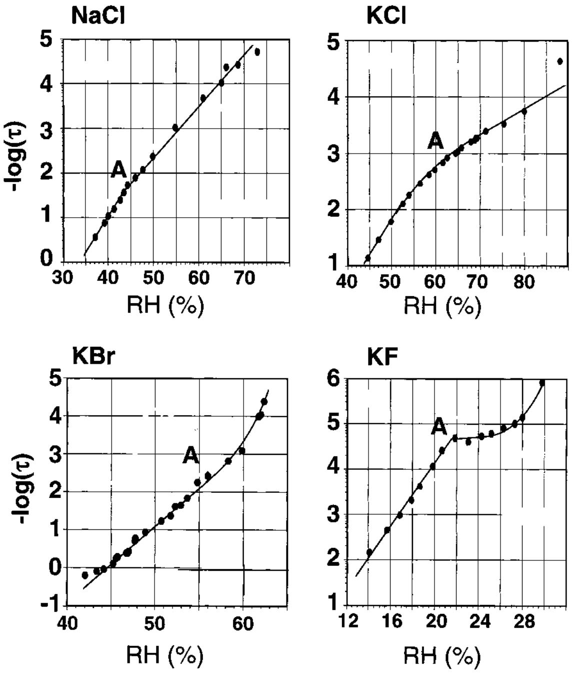

Figure 4. Semilog plot of the time constant τ, obtained as shown in Figure 3, as a function of RH for NaCl, KCl, KBr, and KF. Point A marks the RH value at which a change in the rate of variation is observed. The absolute value of A varies ±5 % in different experiments.

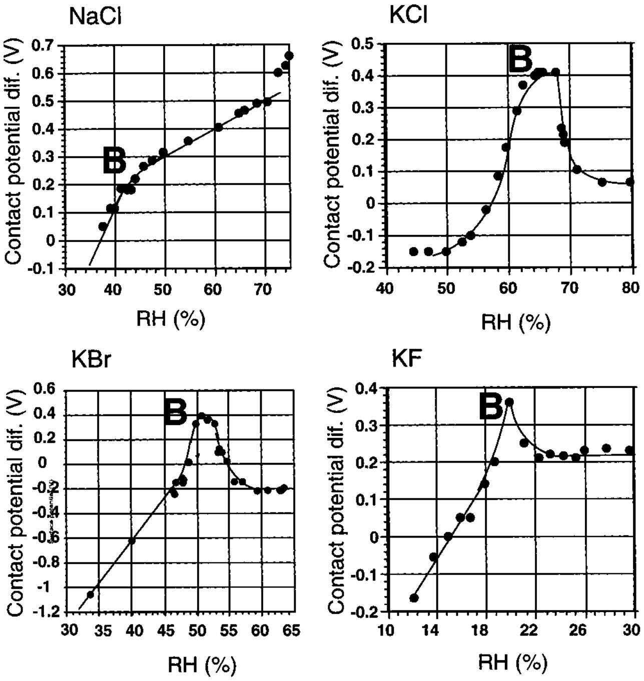

Figure 5. Variation of the contact potential as a function of RH for the four salts. Point B marks the RH value at which a decrease in the rate of change is observed.

metry of the electrostatic attraction when using positive and negative biases. In order to obtain the same attractive force, independent of the sign of the applied voltage, a small offset V_s is applied to compensate for the difference. The measured values of V_s (in the same experiment to determine τ) are shown in Figure 5.

After cleavage at low humidity, the surface is always found to be negatively charged. This negative potential shifts to positive values with increasing humidity. The surface potential of all four salts displays the same general features. Starting from low humidity, there is a monotonous increase of V_s up to a specific point B. After this, the behavior of V_s depends on the salt. For NaCl, the rate of increase of V_s is simply reduced. For the K salts, V_s peaks and then remains constant, or decreases to a plateau at a slightly higher humidity (point B′), as shown in Table 1.

TABLE 1: Relative Humidity (RH) Values (in %) at Which Changes in the Slope of the Response Time (Point A) and Surface Potential (Point B) Occur

	salt			
	NaCl	KF	KCl	KBr
point A	40	20	71	55
point B	46	20	68	52
point B′	NA	22	75	57

The small difference between points A and B is real (in spite of being smaller than the absolute error in RH of ±5 %), since in this experiment τ and V_s are measured simultaneously. The closeness of the two values is, however, remarkable. It indicates that these two parameters are probably related to the same physical process involving the dissolution of surface ions. We will now present the imaging results to correlate them with the topographic changes occurring at the surface.

Surface Imaging

Contact and Noncontact Imaging. The topography of the surface was studied using various AFM imaging modes. The standard AFM contact mode was used to image the "solid" part of the surface, using the example of KBr (Figure 6). Several steps of single and multiple atomic height are observed in these images. At high magnification, the periodic lattice of the salt is routinely imaged.[7] The effect of high humidity is immediately visible in the bottom image of Figure 6, acquired after ~1 h exposure to an RH close to points A/B. The streaks in the image are due to facile damage caused by tip contact at this high RH.

To study the effect of liquid films without perturbation, noncontact SPFM imaging was performed to eliminate the possible influence of the tip on the topography of the wet surface. As seen from eq 1, the images obtained in this way contain three contributions: topography from $f(R/z)$; contact potential from V_s, and electric responsiveness (polarizability) from ϵ. Imaging at either positive or negative bias allows us to separate the contributions of contact potential due to immobile charges or dipoles from topographic and polarizability contributions.

An elegant way to separate the contact potential contribution is to use ac bias modulation and lock-in detection of the first and second harmonic components of the lever oscillation, as shown by Yokoyama et al.[8] The authors named their technique scanning Maxwell stress microscopy (SMSM). The second harmonic signal is a simple consequence of the quadratic dependence of force on the bias. By using the 2ω output of the locking amplifier as the feedback control signal, one obtains an image that contains only contributions from topography and $\epsilon(\omega)$. The lock-in output at ω, on the other hand, contains only the contribution of $\epsilon(\omega)$ and V_s, but not the topography. Finally, the frequency-dependent contribution to the polarizability $\epsilon(\omega)$ can be investigated using different frequencies or in the time domain, as described in the previous section.

Step Motion and Surface Dissolution. An important result obtained using the SPFM imaging mode was the observation of step motion in all four salts. This motion produced rounding of the originally straight steps, which crisscross the surface after cleavage in the dry environment (top image in Figure 6).

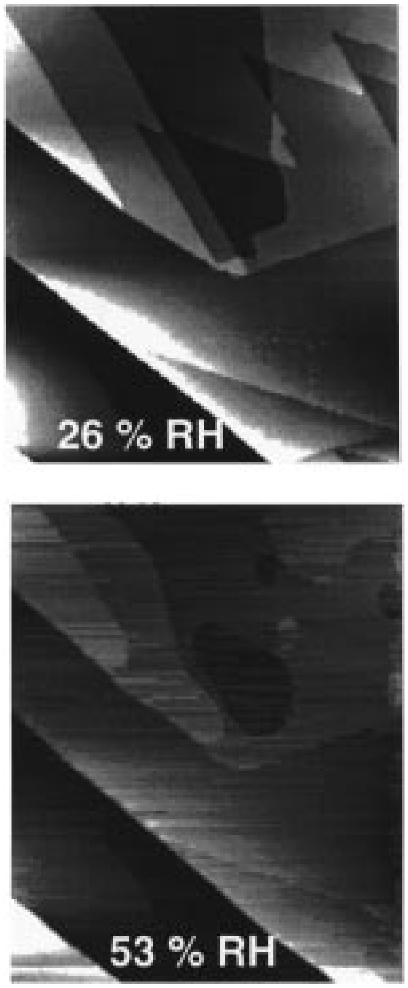

Figure 6. Contact AFM images of KBr. Top: after cleavage under dry conditions (RH = 26%). Straight steps crisscross the surface, forming sharp angles. They result from bulk slippage planes as they intersect with the surface. Bottom: after exposure to 53% RH. The steps have displaced to form rounded terraces.

TABLE 2: Average Relative Humidity (RH) Values (in %, ±5%) at Which Topographic Changes Occur

	salt			
	NaCl	KF	KCl	KBr
start of rapid step motion	40	20	66	55
deliquescence	73	25	87	86

Although motion of monoatomic steps becomes observable even at low humidity, it accelerates greatly when the RH reaches a value close to those of points A or B. For NaCl, this is in agreement with our previous work.[3] Step displacement and rounding become faster with increasing RH up to a critical point, where the images become unstable owing to the formation of a thick liquid film, which is indicative of the dissolution of the substrate. This is the deliquescence point, corresponding to equilibrium between the water vapor and the saturated salt solution. Images showing step motion and substrate dissolution in NaCl were published recently by the authors and will therefore not be shown here. The RH at which these topographic changes occur are given in Table 2 for the four different salts.

Preferential Adsorption of Water at Steps. Another interesting result from the imaging experiments is the observation of a striking enhancement of the step edge contrast in the dc SPFM images when the relative humidity was decreased below point A and/or B. This enhancement (see example in Figure 7, top image) is observed as a protrusion decorating the steps and is observed for both positive and negative tip bias. Its height depends on the RH, reaching a maximum of up to several tens of angstroms at a value of RH about half that of point A. This enhancement could not be observed in contact images acquired under the same conditions. This indicates that the step enhancement could be due to (a) topography from a liquid ribbon decorating the steps, (b) a high value of $\epsilon(\omega)$, or (c) a higher value of the contact potential at the steps.

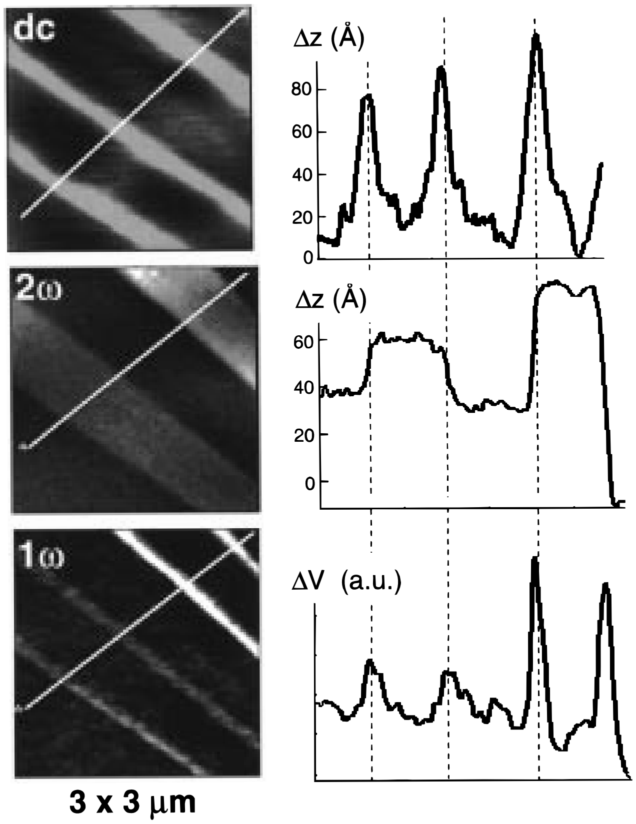

Figure 7. Top: SPFM image in dc mode of a NaCl surface at 22% RH. The contrast is enhanced at the steps owing to the combined action of local surface potential, dielectric contribution, and topography. Center: SPFM image in ac mode (7 kHz) produced by keeping constant the 2ω response amplitude. The image contrast is due to topographic and dielectric contrast but not to variations in the local surface potential. Bottom: image of the amplitude of the 1ω response acquired simultaneously. The contrast is due exclusively to local contact potential. Cursor profiles are shown on the right side.

Step enhancements in SPFM were first observed for NaCl by Dai et al.[3] The present results reproduce these findings and extend them to the other alkali halides. In addition, new experiments using ac bias shed more light on the nature of this phenomenon. In Figure 7, we present images of NaCl in the three electrostatic imaging modes described above. The top image, taken in dc mode, shows the step enhancement when RH = 22%. The center image is from the feedback control signal at 2ω (when $\omega = 7$ kHz). The bottom image is from the 1ω signal amplitude acquired simultaneously with a second lock-in amplifier. As can be clearly seen, the 2ω image displays the topographic features (steps) with no particular enhancement of the edges at the 7 kHz frequency used here. The image is similar to that recorded in contact mode. In the 1ω image, however, the topographic contribution is not present but the step enhancement is very clear. This enhancement appears for NaCl at RH values as low as 19%, reaches its peark at ~25% RH, and disappears at point A/B, i.e., at 40% (±5%) RH.

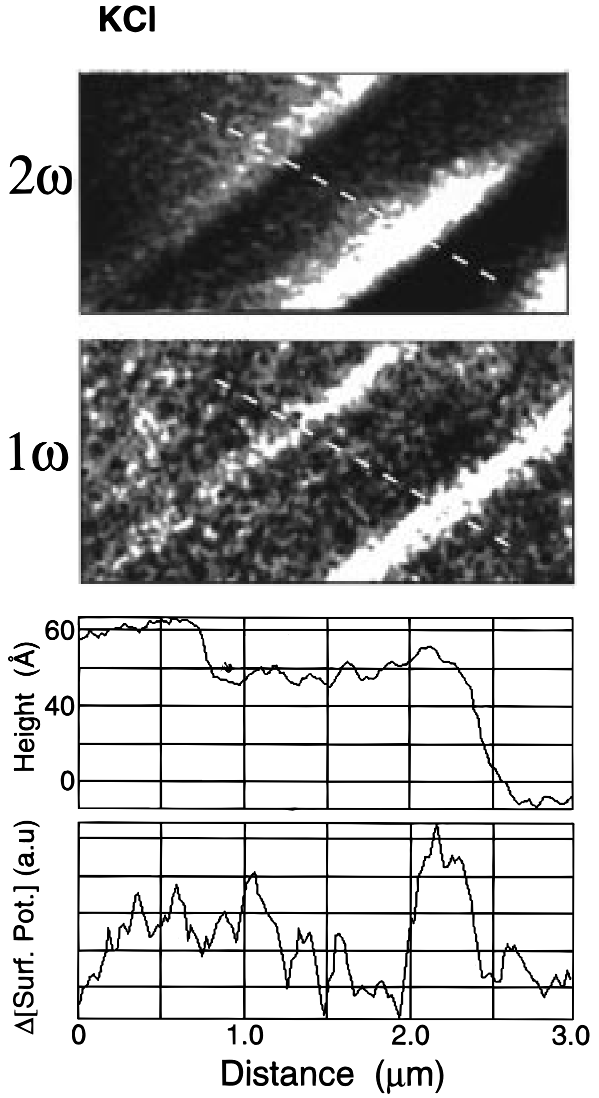

Figure 8. SPFM images of KCl at 41% RH, using ac modulation (7 kHz). Top: constant 2*ω* response amplitude. Center: amplitude of the 1*ω* response acquired simultaneously. Bottom: cursor profiles. Step enhancement is visible in both images, although it is much larger in the 1*ω* image.

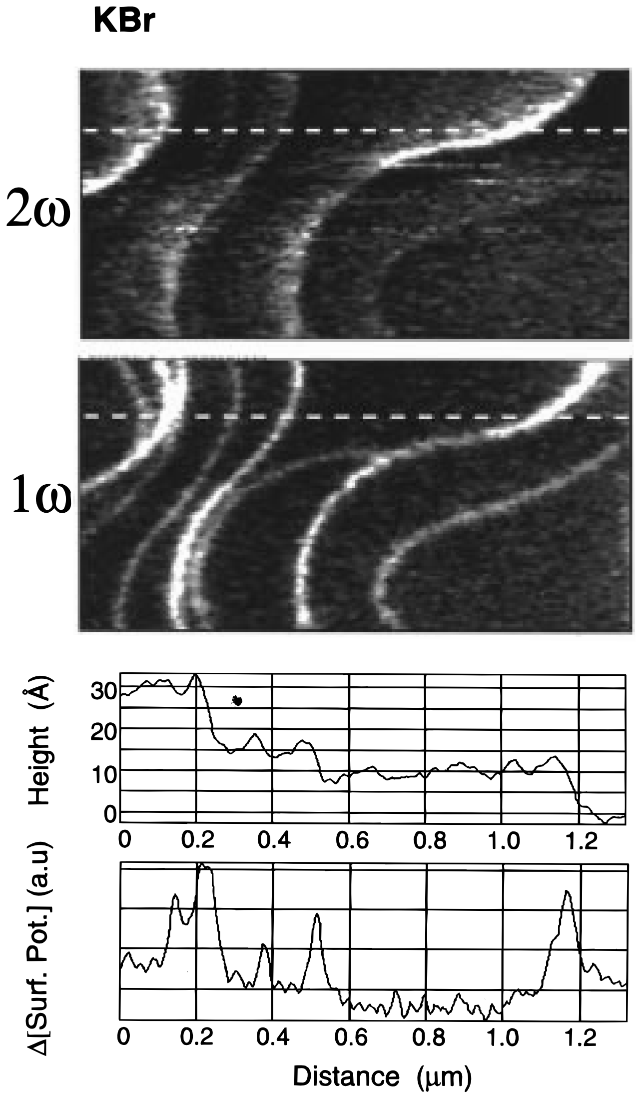

Figure 9. SPFM image of a KBr surface at 30% RH using ac modulation (7 kHz). Top: constant 2*ω* response amplitude. Center: amplitude of the 1*ω* response acquired simultaneously. Bottom: cursor profiles. Step enhancement is also visible in both images although it is much larger in the 1*ω* image.

In similar experiments performed with KCl, we see step enhancement beginning at about the same low RH (15%) and its peak is reached at 30% RH. As for NaCl, enhancement starts to decrease from this point until it disappears at point A/B, which corresponds to 70% (±5%) RH. For this salt, some enhancement close to the steps is also visible on the 2*ω* images, but only in the RH range between 40% and point A. Similar behavior is observed for KBr between 10% RH and point A/B, or 55% RH. Examples for these two salts are shown in Figures 8 and 9.

Discussion

The time dependence of the force between the tip and the surface is the result of charging processes with different time constants. Charge accumulates in the tip as a result of the buildup of ionic charge on the surface underneath the tip (Figure 1), which is the relatively slow process studied here. Another part of the charge, which accumulates much faster, is due to the capacitance of the tip relative to the rest of the apparatus and to the fast part of the substrate polarizability (electronic and lattice ions). Thus, when the bias polarity is reversed, there is an initial fast repulsive contribution that lowers the value of the attractive force and produces the step decrease in force shown in Figure 2. The ion distribution under the tip then rearranges slowly to again reach a stationary value. We will now discuss the functional form of the surface charge distribution and the time dependence of the force.

Contribution of Mobile Ions to the Electrical Polarizability. The mass transfer of hydrated ions moving toward or away from the tip can be described by the Nernst−Planck equation, which includes contributions due to migration, diffusion, and convective motion of the ions

$$\frac{\partial c}{\partial t} + (\vec{v}\cdot\nabla)c = -\mu\vec{\nabla}\cdot(c\vec{E}) - D\Delta c \qquad (2)$$

where c is the concentration of mobile ions, μ the mobility, and D the diffusion coefficient. E is the electric field experienced by the charges. This equation, together with the Gauss law relating E and c, forms a system of differential equations that can be solved for an exact description of the charge distribution underneath the tip. We are not aware of any simple (analytic) solution for these equations, even in the

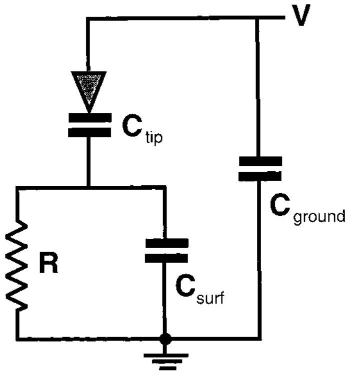

Figure 10. Equivalent RC circuit for the tip, sample, and ground used to describe the time dependence of the surface-induced ionic charge. The resistance *R* is due to the concentration and mobility of solvated ions. C_{surf} is the largest capacitance, on the order of picofarads.

case of a 2D charge distribution with axial symmetry. Therefore we will provide here a simple approximation to the solution.

Since the field is large, we neglect the convection ($v\cdot\nabla$) and thermal diffusion (Δc) terms and take into account only migration. In an even cruder approximation, we can integrate the charge distribution over the region containing the charge accumulated under the tip and only consider total charges. Equation 2 then gives

$$\frac{dq}{dt} = -\mu\cdot\sigma(r) \times 2\pi r E_{||}(r, t) \tag{3}$$

where $\sigma(r)$ is the surface density of charges at a certain distance *r* from the tip/lever assembly. We shall assume in the following that this distance is large enough so that $\sigma(r)$ is simply the surface density of free carriers on the surface far away from the tip. The term $2\pi r E_{||}(r)$ can be regarded as the potential from the charge *q*. We will rewrite it as q/C, where *C* contains all the geometrical factors and is equivalent to a capacitance. The system is similar to an RC circuit where the tip/lever and sample surfaces act as the two plates of a capacitor and where resistance is due to the finite density and velocity of the surface ions. The differential equation governing the charge variation on the surface is thus given by

$$\frac{dq}{dt} = \frac{1}{R}\left(V_0 - \frac{q}{C}\right) \tag{4}$$

where $R = (\sum_i \mu_i \sigma_i)^{-1}$ is an equivalent resistance for the motion of charges on the surface. This produces an exponential relaxation behavior for the charge

$$q(t) = q_0\cdot(1 - e^{-t/\tau}) \tag{5}$$

with a characteristic time $\tau = RC$.

In a real experimental setup, the equivalent circuit is somewhat more complicated, with the capacitance *C* containing contributions from the tip (pyramid and lever)–sample, sample–ground, and tip–ground capacitance (see diagram in Figure 10). As mentioned above, the tip–ground capacitance contribution causes the tip voltage *V* to follow the abrupt square wave pattern shown in Figure 2 (the resistance of the wires is negligible), while the induced charge (through tip–sample and sample–ground capacitance) from diffusing surface ions, and its image, follows eq 5. There is another induced surface charge that is due to the fast part of the dielectric constant (i.e., electronic, dipole, and lattice ions). An electrostatic problem that is conceptually similar is that of a charge in front of a biased conductor,[9] which leads to linear and quadratic terms in $q(t)$. By either using the formula in ref 9 or following the diagram in Figure 10, it is easy to show that the electrostatic force between the tip and surface contains a fast term following the $V(t)$ graph in the top of Figure 2, a *q* term, and a q^2 term, which gives an expression of the type $a\cdot e^{-t/\tau} + b\cdot e^{-2t/\tau} + c$, with $\tau = R(C_{tip} + C_{surf})$. This is the expression that was fitted to the data shown at the bottom of Figure 2 to extract τ.

The capacitance determining the time constant is not only due to the tip apex, which should be on the order of attofarads (10^{-18} F), but to the entire tip assembly (tip pyramid and bending cantilever, which are both on the order of femtofarads (10^{-15} F)), cantilever support (on the order of picofarads (10^{-12} F)), and sample–ground capacitance (also on the order of picofarads). These last two capacitances are the dominant ones and are constant throughout the experiments. Their combined value was measured independently to be 6 pF in our experimental setup. The relative variations of the capacitance that determine the force contrast during SPFM imaging, however, are determined by the closest part, i.e., the tip pyramid. This is, of course, the reason why images with resolution of several tens of nanometers can be obtained. The resistance *R* can be expressed using the above simple model for the mobility of the ions, which yields the following expression for the time constant τ

$$\tau = \frac{C}{\sum \mu_i\cdot\sigma_i} \tag{6}$$

where σ_i and μ_i are the surface concentration and mobility of ions of species *i*.

Since *C* is known by direct measurement, we can obtain the value of the surface resistance *R* from the measured τ. Typical resistance values are found to be on the order of 10^{10} Ω, which corresponds to time constants in the millisecond range. These values are in agreement with the direct current measurements of Hucher et al.[10]

Average Surface Potential and Step Motion. It is a well-known phenomena that the salt surface is always *negatively* charged after cleavage at low humidity. At the surface of ionic crystals, there is an electric dipole layer, the so-called Debye–Frenkel double layer, that is due to the difference between the formation energies of cation and anion vacancies.[11]

As humidity increases, the water molecules adsorb preferentially on the positive ions,[12,13] allowing these charges to be removed from the lattice onto the surface in the form of a solvated ion. This explains why the surface potential shifts to positive values and also explains the increase in surface conductivity.

As we have seen for all the salts studied, a change of slope in the surface potential V_s and surface conductivity R^{-1} vs RH curves occurs at a well-defined humidity value for each salt (points A and B). The difference between these two points is rather small. It is also clear that the change is much stronger in the contact potential curves than in the surface conductivity curves. We can understand this result by considering that they are related to σ and μ in the following way

$$V_s = (\sigma_+ - \sigma_-)\cdot d/\epsilon \quad \text{and} \tag{7}$$

$$R^{-1} = \mu_+\sigma_+ + \mu_-\sigma_- \tag{8}$$

where the + and − subscripts refer to the cation and anion contributions and *d* refers to the average distance of the solvated ions to the surface, which is ~2–3 Å. Below points A and/or

B, it is mostly the σ_+ contribution that is important. After that, both σ_+ and σ_- increase, leading to a large effect on V_s and a smaller effect on R^{-1}.

That changes are observed in so many surface properties in the vicinity of points A and B is truly remarkable and indicates that the surface concentration of water has reached some critical point. Hucher et al.[10] assume that point A corresponds to the completion of a water monolayer. More recently, Peters and Ewing[14] concluded, by using infrared spectroscopy, that the water coverage on NaCl is one monolayer at ~37.5% RH, which is again very close to point A.

We now estimate the number of solvated ions present on the surface at point A, assuming for simplicity that only positive ions are present. We can use the measured values of τ and C to compute R^{-1}, and literature data from bulk-saturated solutions for ion mobility. In the case of NaCl, for example, eq 8 gives a concentration on the order of 10^{17} Na^+ ions/m^2, which is $\sim 10^{-2}$ times the crystal surface concentration of sodium ions. The surface potential change due to these solvated ions is, according to eq 7, ~0.1 V (using $d \sim 2$ Å), which is consistent with the observations. Similar results are obtained for the other salts.

We observed in both contact and noncontact images that step motion increased for all salts when the humidity increases. This increase is very rapid after reaching point A and/or B. In order for step motion to take place, mass transport of both ionic species (cations and anions) must occur. As we have seen, water dissolves mostly positive ions before point B is reached. This explains the slow motion of the steps because of the slow dissolution rate of negative ions at low humidity. The surface potential drop at point B indicates a much higher rate of anion dissolution at this point and explains the rapid step movement observed after point B. The details of this process, however, are different for the Na and K salts: for NaCl, it appears that only a moderate change in the rate of dissolution of both ions occurs, while for the K salts, the change is much more dramatic and includes a net decrease of V_s after point B.

Preferential Dissolution of Cations at Step Edges at Low Humidity. We have seen that, at RH values below point B, surface potential changes are localized at the step edges (Figures 7, 8, and 9). This can be explained by assuming that preferential dissolution of cations occurs at the steps. The solvated ions remain near the negatively charged step edge and create a positive surface dipole, as depicted in the schematic drawing in Figure 11. At humidities below point B, the ionic response time is small enough ($\tau > 1$ ms) that, in the ac images at frequencies >1 kHz, the step dipole appears fixed and produces a strong contrast in the ω images (surface potential). In the 2ω images, which reflect only topography and local polarizability ϵ ($\omega > 7$ KHz), the enhancement is small or not observed. During dc imaging, however, the solvated cations have enough time to move toward or away from the tip so that the step dipole is always of the opposite sign to the tip bias and produces an additional attractive force at the steps.

The preferential accumulation of solvated cations at steps disappears after point B, in agreement with our model in which both + and − ions dissolve at similar rates from this point forward, removing the negative charge accumulated at the steps and triggering rapid step motion.

Model for Surface Conductance as a Function of Water Coverage. Hucher et al.[10] used an empirical exponential dependence of the surface conductivity on water coverage to explain their observed conductivity results vs RH. Subsequent direct measurements of the amount of water adsorbed on the surface have not confirmed this assumption but have provided data on the relation between water coverage and humidity. Here we use this literature data,[12,14] together with our measurements, to model the dissolution process, i.e., the relation between conductivity and water coverage.

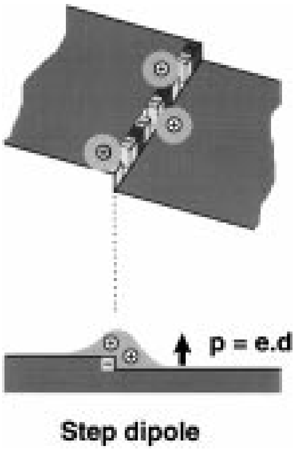

Figure 11. Schematic diagram illustrating the formation of solvated positive ions near the negatively charged steps. This creates a positive surface dipole localized around the steps. The ions can easily follow the changes in tip bias that occur over long time periods (>1−10 ms), but with difficulty at rates of several kilohertz.

We assume that the cations are freed from the lattice (i.e., become solvated) when they acquire at least k_0 water molecules. We further assume that we have n possible adsorption sites (n cations on the crystal surface) on which we randomly distribute (adsorb) p water molecules. The probability of having a site covered by k water molecules is

$$P(k) = \mathrm{C}_p^k\left(\frac{1}{n}\right)^k\left(\frac{n-1}{n}\right)^{p-k} \tag{9}$$

The number of released ions as a function of coverage ($\theta = p/n$) can be calculated by summing the probabilities of having k larger than a threshold value k_0. One then obtains the following expression for the fraction of solvated ions as a function of θ

$$P(\theta) = 1 - \exp(-\theta)\cdot\sum_{i=1}^{k_0-1}\left(\frac{\theta^i}{i!}\right) \tag{10}$$

The results of this equation have been plotted in Figure 12, together with the experimental conductivity data for NaCl and KCl salts. A linear dependence of coverage between RH values of 20−40% was assumed.[14] For KCl, a similar dependence was used (0-1 ML for 30-65% RH). We can see that, for NaCl, $k_0 = 6$ provides a reasonable fit, considering the many orders of magnitude covered. This value of k_0 is close to the hydration number of sodium ions in solution. For KCl, an even better fit was obtained for $k_0 = 5$, a value that is in turn in agreement with the larger size of the K^+ ion. The coverage of free ions predicted by this model (right ordinate in the graphs) agrees well with our previous estimates based on the observed values of V_s and R^{-1}.

Summary and Conclusions

By studying the evolution of surface potential and surface conductance with relative humidity using the various AFM

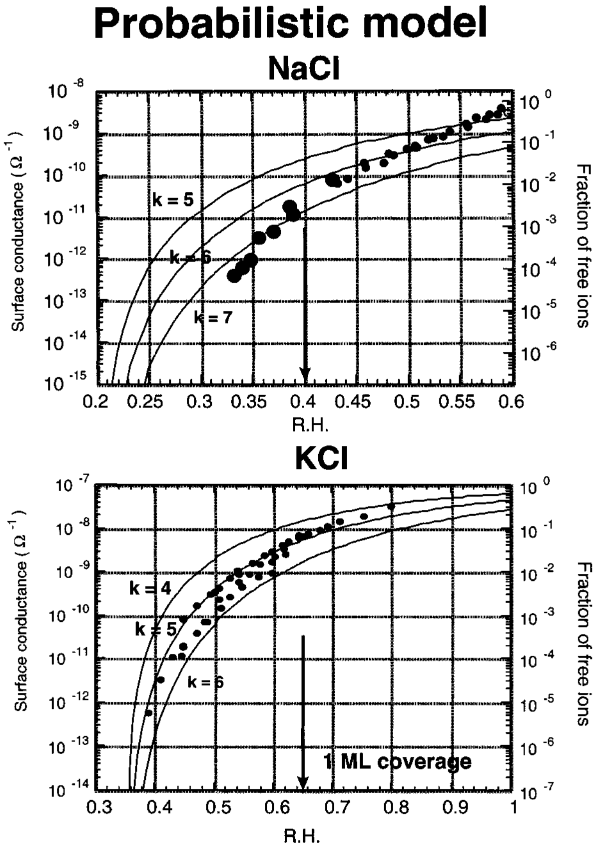

Figure 12. Comparison of the measured surface conductivity (from Figure 4) for NaCl (top) and KCl (bottom) with the predictions from the probabilistic model discussed in the text. In this model, an ion becomes solvated when it acquires a minimum of k_0 water molecules. For NaCl the best fit is for $k_0 = 6$, while for KCl it is $k_0 = 5$.

imaging modes (contact, and electrostatic at dc and ac), we have gained a detailed understanding of the process of adsorption of water on the alkali halide surfaces.

The alkali halide surfaces show a negative surface potential after cleavage at low RH (<20 %), which can be explained by the Debye–Frenkel vacancy defect model.

The surface ionic conductance increases quasi-exponentially with humidity owing to the rapid increase in the number of dissolved ions. There is a change in the rate of increase at a particular humidity value (point A).

Surface potential change measurements indicate that positive ions dissolve preferentially at low humidity below a specific value (point B) that is only slightly different from point A. The dissolution takes place preferentially at the steps, which become decorated with solvated cations and thus acquire a positive potential.

For the salts studied here, anion dissolution accelerates upon reaching point B. After this point, the surface potential becomes homogeneous over the surface and mass transfer becomes fast enough to produce rapid (on the scale of minutes) motion of the steps. The surface concentration of solvated cations at point B is on the order of 1% of the surface density, and their mobility is on the same order of magnitude as that in saturated solutions.

The surface step structure collapses at high humidity, when the deliquescence point of the salt is reached. A thick liquid film is formed at this time.

A simple probabilistic model, together with a linear relation between water coverage and humidity, is sufficient to explain the observed changes in conductivity over many orders of magnitude. This model assumes that cations become solvated when they acquire a minimum number of water molecules. This number is six for NaCl and five for KCl.

Acknowledgment. This work was supported by the Lawrence Berkeley National laboratory through the Director, Office of Energy Research, Basic Energy Science, Materials Science Division of the U.S. Department of Energy, under Contract DE-AC03-76SF00098. We thank A. Artsyukhovich for his help in the measurement of the capacitance of the system and S. Pouget for her help in the probability calculations. M.L. acknowledges financial support from the Ministry of Education of Spain, Project PB 92-0269 CICYT, and F.R. acknowledges support from a NATO grant.

References and Notes

(1) Sedunov, Yu. S. *Physics of Drop Formation in the Atmosphere*; John Wiley: New York, 1974.

(2) *Atmospheric Aerosols and Nucleation*; Proceedings of the Twelfth International Conference on Atmospheric Aerosols; Wagner, P. E., Vali, G., Eds.; Springer-Verlag: New York, 1988.

(3) Dai, Q.; Hu, J.; Salmeron, M. *J. Phys. Chem. B* **1997**, *101*, 1994.

(4) Hu, J.; Xiao, X.-d.; Ogletree, D. F.; Salmeron, M. *Science* **1995**, *268*, 267.

(5) Hu, J.; Xiao, X.-d.; Ogletree, D. F.; Salmeron, M. *Appl. Phys. Lett.* **1995**, *67*, 476.

(6) Xu, L.; Lio, A.; Hu, J.; Ogletree, D. F.; Salmeron, M. *J. Phys. Chem. B* **1998**, *102*, 540.

(7) Carpick, R. W.; Dai, Q.; Ogletree, D. F.; Salmeron, M. *Tribol. Lett.*, in press.

(8) Yokoyama, U. H.; Inoue, T. *Thin Films* **1994**, *242*, 33.

(9) Jackson, J. D. *Classical Electrodynamics*, 2nd ed.; John Wiley & Sons: New York, 1975.

(10) Hucher, M.; Oberlin, A.; Hogart, R. *Bull. Soc. Fr. Mineral. Cristallogr.* **1967**, *90*, 320.

(11) Tanibayashi, M. *J. Phys. Soc. Jpn.* **1994**, *63*, 168.

(12) Barraclough, P. B.; Hall, P. G. *Surf. Sci.* **1974**, *46*, 393.

(13) Estel, J.; Hoinkes, H.; Kaarman, H.; Nahr, H.; Wilsh, H. *Surf. Sci.* **1976**, *54*, 393.

(14) Peters, S. J.; Ewing, G. E. *Langmuir* **1997**, *13*, 6345.